ABSTRACT

Title of Thesis: INSTRUMENTATION AND AUTOMATION FOR STIMULATED BRILLOUIN SPECTROSCOPY

Eric C. Frank, Master of Science, 2023

Thesis directed by: Professor Giuliano Scarcelli,
Department of Bioengineering

The use of Brillouin spectroscopy for noninvasive probing of the mechanical properties of biologically relevant materials shows great promise. Stimulated Brillouin scattering (SBS) spectroscopy has the potential to significantly improve measurement speed and resolution by amplifying the scattered signal resonantly. However, current SBS spectrometers have been limited by fundamental and practical constraints in detection parameters. Here, we develop and demonstrate a novel LabVIEW-automated SBS instrumentation scheme in which a number of instruments that otherwise operate independently are automatized and synchronized from a singular LabVIEW program with emphasis on the user interface. Additionally, localization theory, originating from fluorescence-based super resolution microscopy techniques, is applied to the acquisition of SBS spectra, and experimentally demonstrated using this instrumentation scheme, resulting in spectra being acquired an order of magnitude faster while maintaining performances in terms of signal to noise ratio (SNR) and measurement precision.

INSTRUMENTATION AND AUTOMATION FOR STIMULATED BRILLOUIN SPECTROSCOPY

by Eric Frank

Thesis submitted to the Faculty of the Graduate school of the
University of Maryland, College Park, in partial fulfillment
of the requirements for the degree of
Master of Science
2023

Advisory committee:
Professor Giuliano Scarcelli, Chair
Professor Ian White
Professor William Bentley

Acknowledgements

Words cannot truly express the gratitude I have for those for whom this work would not be possible. I'll try anyway. First, I would like to thank my parents for their unceasing support of me in my endeavors. Their financial and emotional support were crucial during my time at the University of Maryland.

Next, I would like to thank Giuliano Scarcelli, who by a stroke of generosity, took me on as a student research assistant. I will always cherish the scientific discussions we had, and I am grateful for the endless series of opportunities that he's provided me.

I would also like to extend my sincerest thanks to my mentor, Giulia Zanini. Without her, this project would not exist. Her patience, organization, and guidance critical to the development of this project. This thesis is as much her work as it was mine.

The Scarcelli Bio optics lab has been, in some respect, my home away from home, and I could ask for no better colleagues: Justin, Claudia, Jake, Raymundo, Romanus, Chenchen, Milos, Tony, Josh, Christina and Maggie. Through trials and tribulations, over coffee and ramen, in the early morning and after the sun has set, they have been there every step of the way, providing laughter, engaging discussion, and camaraderie.

Finally, I would like to thank the Fischell department of Bioengineering as a whole. The faculty and staff made my time at Maryland a thoroughly enjoyable one. It's a bittersweet moment to say farewell to them all, but this is truly the culmination of their efforts and mine.

Thank you everyone. I'm proud to have been a part of this school, this department, and this lab. I am proud to be a Bioengineering Terp.

Table of Contents

List of figures

1. Brillouin Spectroscopy in Biomedicine

1.1 Brillouin Scattering

Brillouin Light Scattering (BLS) is a phenomenon characterized by the inelastic scattering of photons when interacting with density fluctuations, or acoustic phonons in a material (Brillouin, 1922). These scattered photons undergo a frequency shift with a Lorentzian distribution described by equation 1:

$$v_B = 2n\frac{v_s}{c}vsin(\frac{\theta}{2}) \quad (1)$$

Where v_B is the central shift of the Lorentzian, n is the refractive index of the material, v_s is the speed of sound, c is the speed of light, v is the frequency of the photons incident to the material, and θ is the angle at which the photons are scattered. The linewidth of the scattered photon Lorentzian distribution can be described by equation 2:

$$\Gamma_B = 2\pi(\frac{2nv}{c}sin(\frac{\theta}{2}))^2\Gamma' \quad (2)$$

Where Γ' is the damping parameter. The properties of the scattered photons directly relate to the mechanical properties of the material the photons interact with. In particular, in backscattering geometry (θ=180°), the real and imaginary components of the longitudinal modulus, M' and M" respectively, can be calculated via equations 3 and 4:

$$M' = \rho {v_s}^2 = \frac{\rho}{n^2}\frac{{v_b}^2c^2}{4v^2} \quad (3)$$

$$M" = \rho {v_s}^2 \frac{\Gamma_B}{v_B} = \frac{\rho}{n^2}\frac{v_b \ \Gamma_B \ c^2}{4v^2} \quad (4)$$

Where ρ is the density of the material (Boyd, 2020). The real component of the longitudinal modulus M' has been shown in biological materials to have an empirical correlation to the Young's modulus, E, which determines the stiffness of a material (Scarcelli et al., 2011, 2015).

1.2 Brillouin Spectroscopy

Optical spectroscopy utilizes light dispersive elements along with a photon detector to spatially separate light into its spectral components. Brillouin spectroscopy is no different in this regard. In the past two decades, Brillouin spectroscopy techniques have been refined through developments involving virtually imaged phased array (VIPA) etalons, which were first introduced in 2008 (Scarcelli & Yun, 2008). The VIPA serves as a spectral dispersive element; photons that enter the VIPA bounce between the highly reflective parallel surfaces. Photons of differing frequency are spatially dispersed and collected by a camera. The position of the photons that reach the camera is representative of the frequency of those photons. Photons that gain or lose frequency from Brillouin scattering therefore are collected as a binned Lorentzian pixel on the camera. This methodology has proven adept at achieving good spectral extinction and sub GHz spectral resolution (Berghaus et al., 2015). Cross axial VIPA spectroscopy, in which two VIPA etalons are placed in series, has become a prevalent configuration, as it further improves spectral extinction and resolution (Scarcelli & Yun, 2011). However, despite improvements in the processing of the scattered light, spontaneous Brillouin spectroscopy is still dependent on weak spontaneous scattering, which necessitates high exposure times (20-100 ms) and illumination power (Nikolić & Scarcelli, 2019; Zhang & Scarcelli, 2021). Achieving faster spectral acquisition times necessitates a novel spectroscopy scheme independent of weak spontaneous scattering.

2. Stimulated Brillouin Instrumentation

2.1 Stimulated Brillouin Spectroscopy

Stimulated Brillouin spectroscopy takes advantage of stimulated Brillouin scattering (SBS). In stimulated Brillouin scattering, rather than photons interacting with the acoustic phonons generated through spontaneous thermal fluctuations, the phonon is induced through the resonance of a counterpropagating pump and probe beam of frequencies ω1 and ω2. When the beat frequency of the pump and probe beam equals the frequency of the acoustic phonon, the probe beam experiences an exponential gain in transmission due to resonance (Remer et al., 2020; Remer & Bilenca, 2016). If the probe beam is scanned in frequency, the resulting transmitted beam will therefore construct a Lorentzian Brillouin spectrum with peak position at the Brillouin shift frequency v_B (Figure 1).

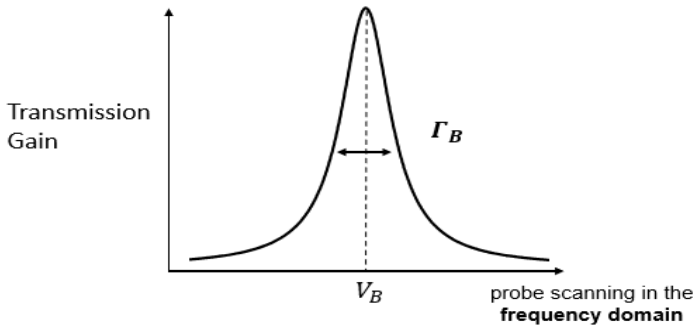

Figure 1. Graph of frequency versus probe laser transmission gain. When the probe laser frequency is scanned around V_B, the transmitted probe beam experiences an increase in transmission exhibiting a Lorentzian distribution.

2.2 Localization Theory

The analysis of the Lorentzian Brillouin peak observed in SBS is fundamentally a localization problem. In recent times, localization problems have garnered significant interest primarily due to their crucial role in advancing super-resolution microscopy methods, like photoactivated localization microscopy (PALM) and stochastic optical reconstruction microscopy (STORM). These techniques involve estimating the location of fluorescent probes by utilizing fitting algorithms on 2D images that are limited by diffraction. Localization microscopy is founded on the principle that, provided an adequate number of photons, the center position of sparsely distributed, sub-resolved objects can be accurately determined without regard to their size being much smaller than the point spread function (PSF) of the microscope. (Deschout et al., 2014; Thompson et al., 2002). The error in localization in 1D follows equation 5:

$$\langle (\Delta x)^2 \rangle = \frac{s^2 + a^2/12}{N} + \frac{4\sqrt{\pi}\, s^3 b^2}{aN^2} \tag{5}$$

Where s is the PSF, a is the camera pixel size, $\boldsymbol{N}$ is the number of photons, b is the number of background noise photons, and Δx is the error in the position of the super resolved object.

This localization theory can be applied to Brillouin peak localization through equation 6:

$$(\delta \nu_B)^2 = \frac{\Gamma_B^2 + Ba^2}{N} + \frac{4\sqrt{\pi}\Gamma_B^3 b^2}{aN^2} \tag{6}$$

Where Γ_B is the natural Brillouin linewidth, N is the total number of Brillouin photons, B is a broadening factor, which describes the error which accumulates as the channel size becomes larger than the natural linewidth Γ_B, a is the spectral channel size - the size of the binning frequency window analogous to pixel size - and b is the number of background noise photons.

Equation 6 can be further factorized into equation 7:

$$\delta\nu_B = \frac{\Gamma_B}{\sqrt{N}}\sqrt{1 + B\left(\frac{a}{\Gamma_B}\right)^2 + \frac{4\sqrt{\pi}b^2}{N}\frac{1}{a/\Gamma_B}} \tag{7}$$

The effect the broadening has on the measured linewidth can be modeled by equation 8:

$$\Gamma = \sqrt{\Gamma_B^2 + Ba^2} \tag{8}$$

Previous literature (Zanini & Scarcelli, 2022) on localization theory for use in SBS used simulated data to characterize the relationship between peak position error and the channel size (Figure 2), and found that the optimal channel size, corresponding to the highest precision and SNR follows equation 9:

$$(a/\Gamma_B)^3_{min} = \frac{2\sqrt{\pi}b^2}{BN} \tag{9}$$

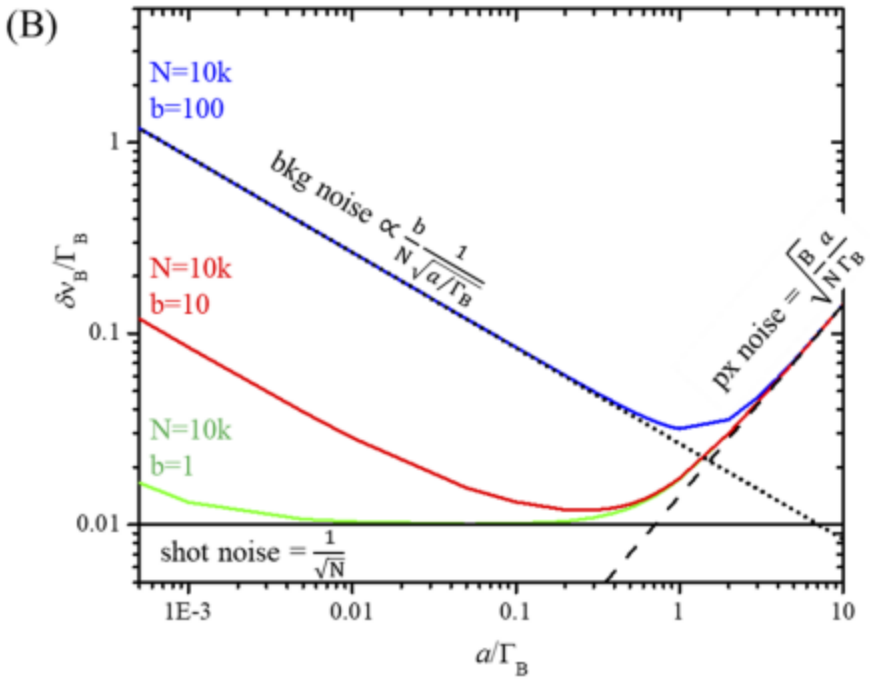

Figure 2. Simulated data sourced from Figure 1b of (Zanini & Scarcelli, 2022), demonstrating the relationship between normalized channel size and the normalized precision for various background noise photon contributions.

The importance of devising an appropriate detection system for SBS spectroscopy based on different experimental conditions, such as the number of signal and background noise photons, is highlighted by the theory. This can result in noteworthy enhancements in SNR and measurement precision. Emphasis should be placed on optimizing signal collection, which can be accomplished by developing an acquisition system with adjustable spectral channel size that aligns with the particular experimental parameters.

2.3 SBS Instrumentation

An instrumentation scheme was devised to build off of previous work in constructing an SBS spectrometer (Zanini & Scarcelli, 2022). Most components of the optical setup were carried over

from this previous work (Figure 3). The SBS spectrometer comprises two counterpropagating CW single-frequency tunable lasers at 780 nm, with a 100 kHz linewidth and 30-50 GHz tunability range. One laser serves as the pump beam (Toptica TA Pro), and the other as the probe beam (Toptica DL Pro). The pump beam is locked to a Rubidium-85 absorption peak via a built-in locking module in the TA Pro. The frequency of the pump beam is modulated by an acousto-optic modulator at 1 MHz (AOMO 3080-125, Crystal Technology, Inc.). The beat frequency of the pump and probe beam is collected and computed by a signal analyzer (CXA Signal Analyzer, Keysight), which is used to calibrate the frequency axis of the collected spectra whilethe probe beam is scanned in frequency around the resonance of the acoustic wave of the sample. A setting in the DL Pro called “Analog Remote Control” (ARC) allows for direct control of the laser frequency via a voltage provided to a BNC connector on the instrument. The frequency of the probe beam is scanned by sending a voltage ramp from a National Instruments Data Acquisition Card (niDAQ USB-6212, National Instruments). The probe beam transmitted through the sample passes through a hot Rb85 vapor cell (Precision Glassblowing) to filter stray pump photons, and is subsequently measured by a photodetector (PDA36A2, Thorlabs). The signal then then is electronically filtered by a bias tee (ZFBT-4R2GW+, MiniCircuits), where its DC and AC components are separated. The SBS signal is then extracted from the total probe transmission via a lock-in amplifier (LIA, UHF, Zurich Instruments) referenced at the pump modulation frequency (1 MHz). The SBS signal is the output from the LIA, which is then sampled by the DAQ. The integration time of the LIA, τ_{LIA}, is the duration that the AC signal is sampled and integrated for, and its duration determines the channel size.

The DAQ synchronizes the voltage ramp to the probe laser, and the sampling of the DC voltage (from the bias tee) and of the LIA signal. The maximum sampling rate of the DAQ is 400k

samples/second; for each N signals read simultaneously, the number of samples per second becomes 400k/N samples/second. In this configuration, with the DAQ reading 3 voltages, the actual maximum sampling rate of the DAQ is 133k samples/second. Sampled points are streamed via USB to a LabVIEW application on a computer. A CMOS camera (Basler) is used to take brightfield images of the samples under the microscope.

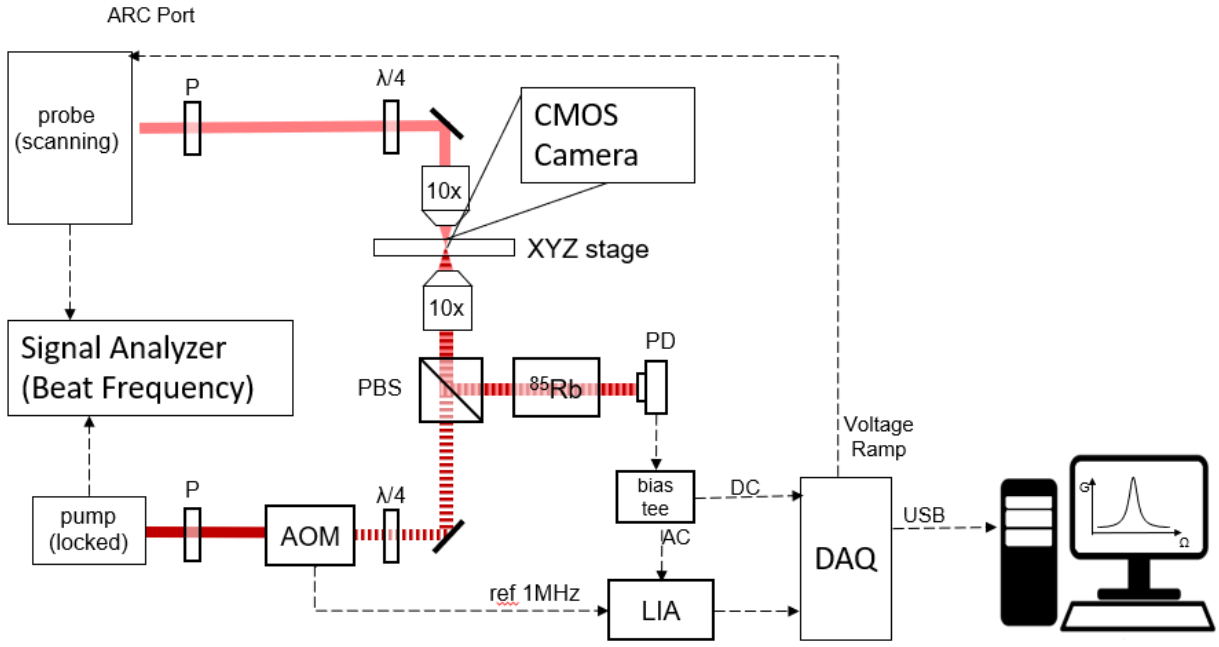

Figure 3. Schematic of optical setup and electronic instrumentation. Dashed black lines represent electric signal, either of a digital communications protocol or analog signal. Dark red represents the pump beam, and light red represents the probe beam. The dashed red lines represent the beam(s) after undergoing a modulation in frequency. P: polarizer, λ/4: quarter-wave plate, AOM: acousto-optic modulator, PBS: polarizing beam splitter, PD: photodetector, LIA: lock-in amplifier, DAQ: Data Acquisition Card

In the previous instrumentation scheme, instead of a DAQ acquiring data, SBS signal was sampled by a module in the DL pro, though its capabilities were notably poor in this respect, having a hard limit of a minimum of 1000 points sampled per spectra and a 200k sample/s maximum sampling rate (Zanini & Scarcelli, 2022). Additionally, the DL pro managed the voltage scan internally rather than receiving a voltage ramp through the ARC. The addition of

the novel elements to the scheme, such as the DAQ, the signal analyzer, and the CMOS, presented an opportunity to better fine tune the synchronization of these to improve setup efficacy using software automation and synchronization.

2.3 LabVIEW Automation of SBS

2.3.1 LabVIEW Overview

Automation of the instrumentation comprising the setup was achieved through software development of an application coded in National Instrument's LabVIEW. LabVIEW is a graphical programming language with origins in automation and data acquisition, designed to resemble a flow diagram to provide a user-friendly environment aiding both development and use. Compared to other development environments such as C++, LabVIEW offers various benefits such as streamlined network communication, pre-built implementation of common communication protocols like RS232, GPIB and VISA, powerful tools for process control and data fitting, fast and easy user interface creation, and an efficient code execution environment. Each LabVIEW program is called a "Virtual Instrument" or "VI." The LabVIEW development environment for VI consists of a "front panel" and a "block diagram." The front panel is the Graphical User Interface (GUI) and contains two types of elements: "controls" and "indicators". The block diagram refers to the executing code, where communication with physical instruments, data processing, and fileIO occurs. Controls are front panel elements which the user can update in live time, inputting values during or before execution of the program which then can affect other variables during the execution of the program or the operation of a physical instrument, e.g. changing the value of a numeric control to affect the exposure time of a camera, or a button that when clicked opens or closes a shutter. Indicators are front panel elements that

display data following updates to that variable in the block diagram during execution. Whenever a control or indicator is added to the front panel, a corresponding control or indicator variable is created in the block diagram, allowing data to flow from the control to the rest of the program, and data to flow from the rest of the program into an indicator (Elliott et al., 2007; Kodosky, 2020). LabVIEW programs have been designed for data acquisition in a wide range of fields, such as measuring the vibration of electric transformers (Thinh et al., 2023), meteorological phenomena (Benghanem, 2009), and real time bolometer tomography (Giannone et al., 2011).

In the Scarcelli Bio Optics lab, LabVIEW has been used to develop a wide range of applications to acquire and display data pertaining to Brillouin spectroscopy. Confocal Brillouin spectroscopy was developed using a LabVIEW application to manage the synchronization of EMCCD cameras and the microscope stage (Scarcelli et al., 2015). LabVIEW software was similarly developed to implement a time lapse and raster scanning protocol to map neural tube closure of embryos (Handler et al., 2023). Additionally, LabVIEW has been used to develop data acquisition and synchronization software for the use of a Brillouin-based flow cytometer (Zhang et al., 2017).

2.3.2 LabVIEW Software Architecture

The LabVIEW application developed for use in this instrumentation scheme is based on a consumer-producer architecture with multiple parallel loops allowing sections of the code to operate independent of the execution speed of one another (Zhi-yu, 2016). From the top down, there are three separate while loops (Figure 4): a main state machine, a CMOS/Camera control loop (Figure 5), and a stage operation loop (Figure 6).

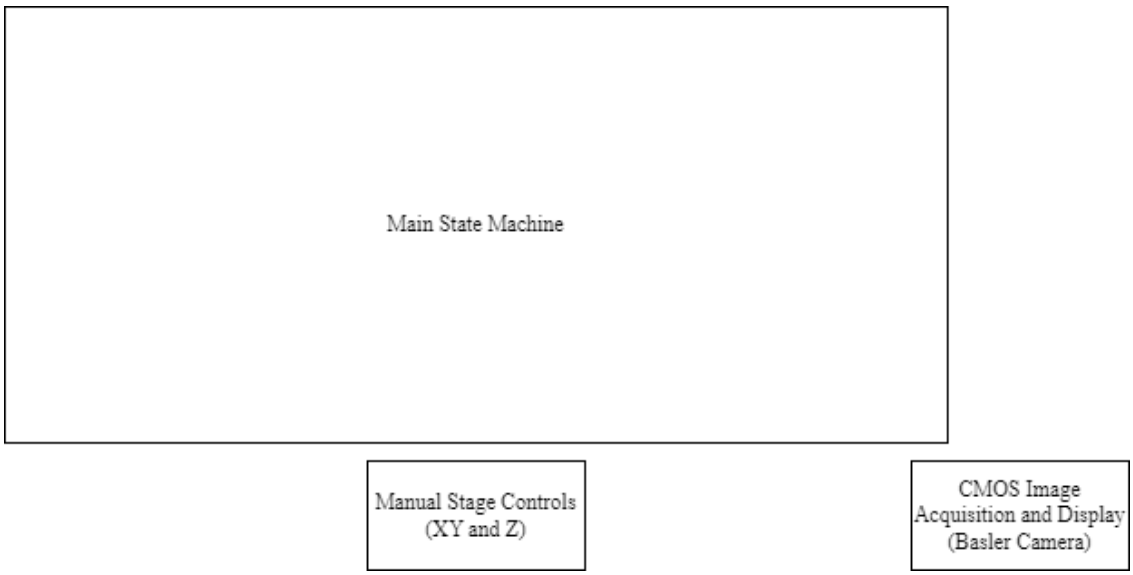

Figure 4. Overview diagram of LabVIEW virtual instrument architecture. Each box represents a while loop, labels designating the functions of that loop. Parallel while loops permit operability of each loop independent of the execution of the other loops. Graphical User Interface (GUI) functionality is improved through the use of parallel loops, as the user can, for example, operate the stage or camera regardless of the current state the main loop is in.

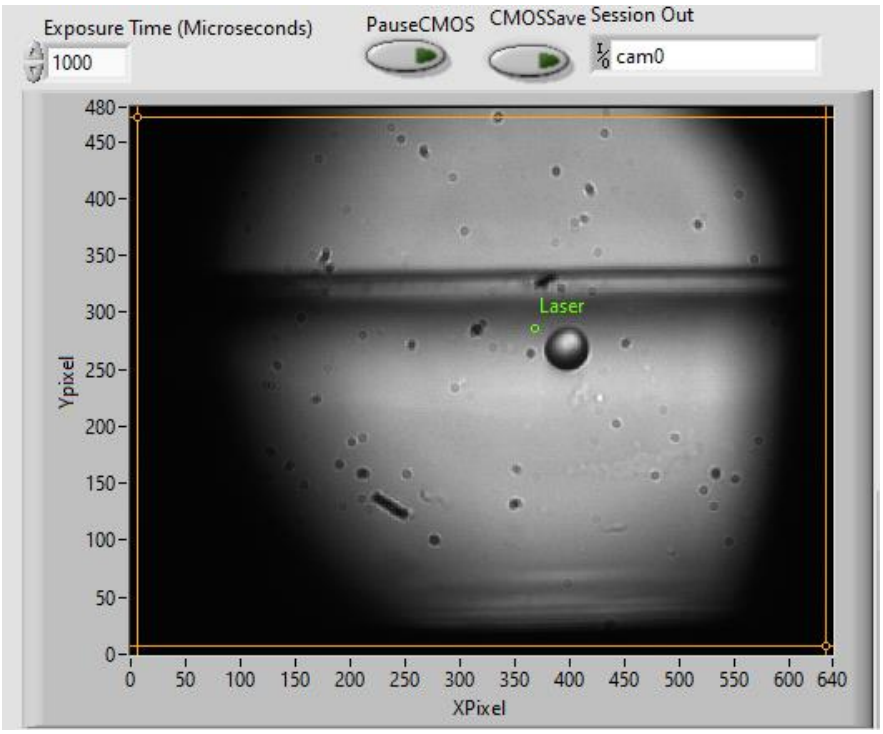

Figure 5. GUI image of CMOS imaging instrumentation. The user may alter the exposure time of the image using the “Exposure time (Microseconds)” front panel control. Clicking the “PauseCMOS" button halts camera acquisition until it is unclicked. The “CMOSSave” button streams and saves the 2D array of the CMOS image into the National Instruments proprietary Technical Data Management Streaming (TDMS) file format. The green “Laser” circular cursor on the image display is used as a reference; the user can freely drag this marker using the mouse cursor to calibrate the position of the laser relative to the image frame. The current image displayed is that of a 10-13 micron polystyrene bead flowing through a 100x100 micron microfluidic channel.

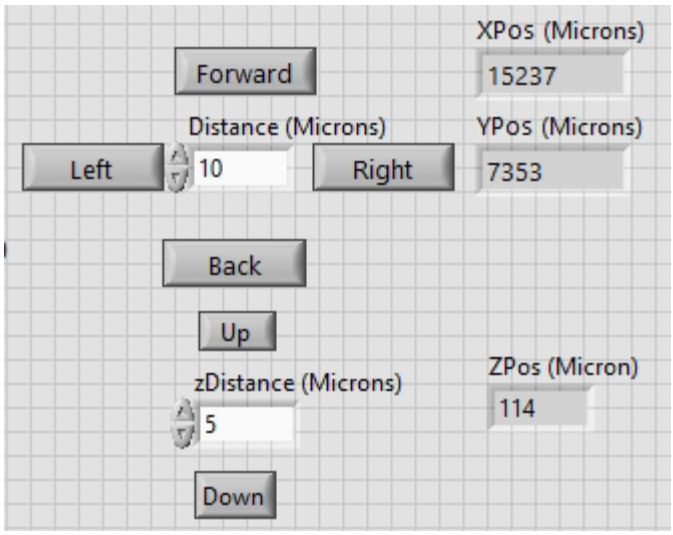

Figure 6. GUI image of stage controls. The user may input an integer into the "Distance (Microns)" control. Upon clicking the buttons marked "Forward" or "Back," the stage will move in the positive or negative Y direction, respectively, the number of microns inputted in the "Distance (Microns)" control. Similarly, upon clicking the buttons marked "Right" or "Left," the stage will move in the positive or negative X direction, respectively, the number of microns inputted in the "Distance (Microns)" control. The "zDistance" control works almost identically, with the stage moving in the positive or negative direction the amount input into the control upon clicking the "Up" or "Down" button respectively. All changes in the X, Y, or Z position of the stage are monitored and reported through the "XPos", "Ypos", and "Zpos" front panel indicators.

Within the main state machine are a number of states, controlled by a case selector variable. Each state refers to a designated phase of the main state machine. The execution of any given state is at the exclusion of the execution of any other state. There are four possible states of the main state machine: Init, Run, Acquisition, and Exit (Figure 7). The Init case handles the start of the program; it initializes variables and opens up communications with the DLC pro, the Prior stage, the Basler camera, and the signal analyzer. The Run case is the continuous usage case of the program; here, the user can adjust most GUI elements, operate a simple voltage scan (Figure 8) to visualize the signal, perform a calibration to match the scanned beat frequency to the voltage ramp sent by the DAQ (Figure 9), and/or adjust parameters and settings for a dedicated acquisition.

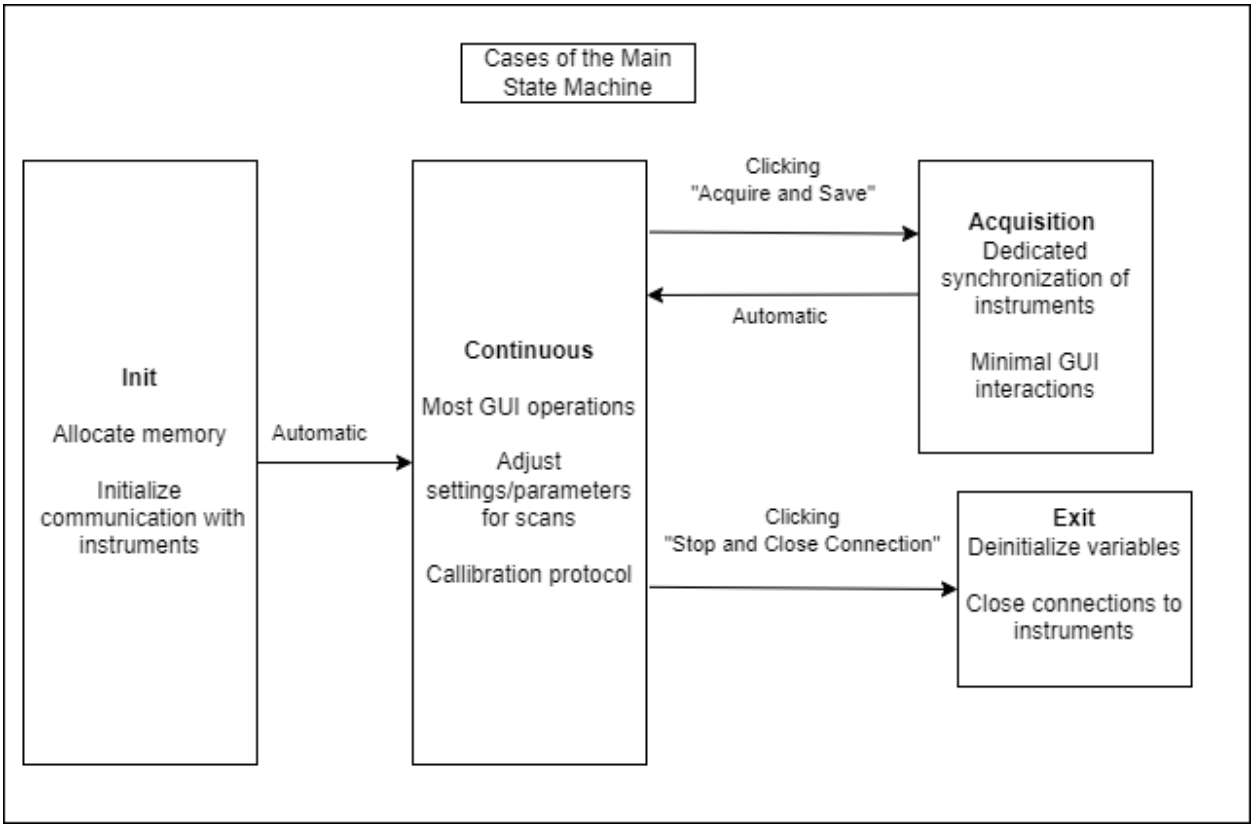

Figure 7. Diagram of the cases of the main state machine and the criteria to switch from one case to another (marked with an arrow).

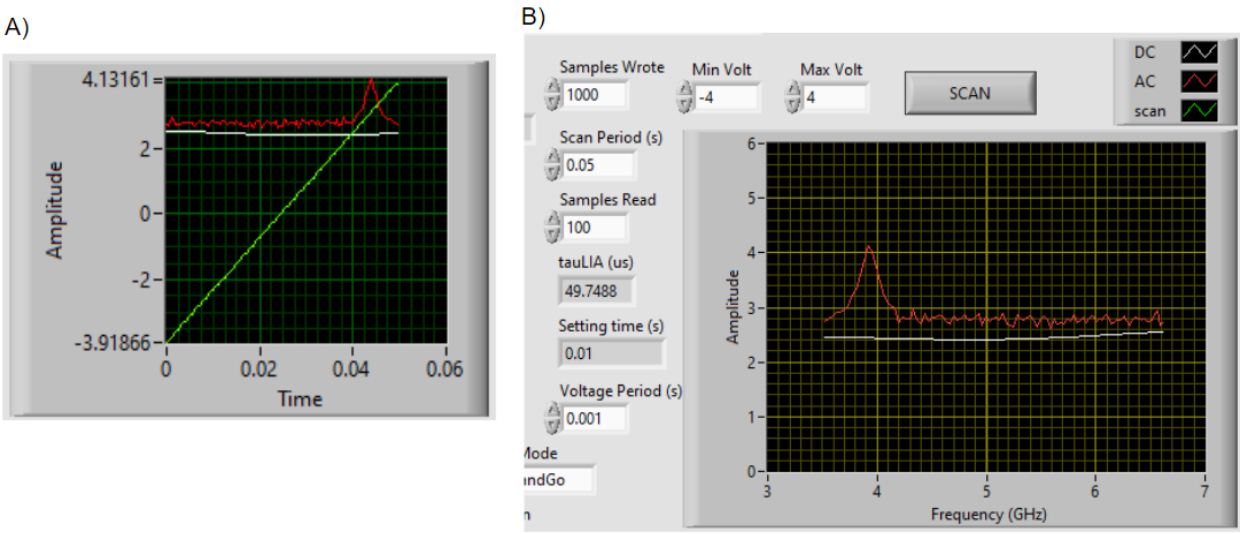

Figure 8. Front panel GUI indicator elements of the continuous running scan. A) raw scan indicator. In red: the lock-in amplifier signal as read by the data acquisition card. In green: the output voltage from the DAQ that serves as the voltage ramp to sweep the frequency of the probe laser. In white: the DC voltage used to normalize the SBS signal.e B) XY Plot where the x axis is the frequency of the laser (if the calibration has been run) or the voltage sweep (if not). During the continuous case of the program, the user can click the “Scan” button, and a voltage scan will be initiated by the DAQ. Various parameters of the analog voltage input and output scan can be modified, such as the period of the voltage ramp, the number of samples per analog input acquired by the DAQ, the minimum and maximum voltages of the voltage ramp, and the resolution of the voltage ramp.

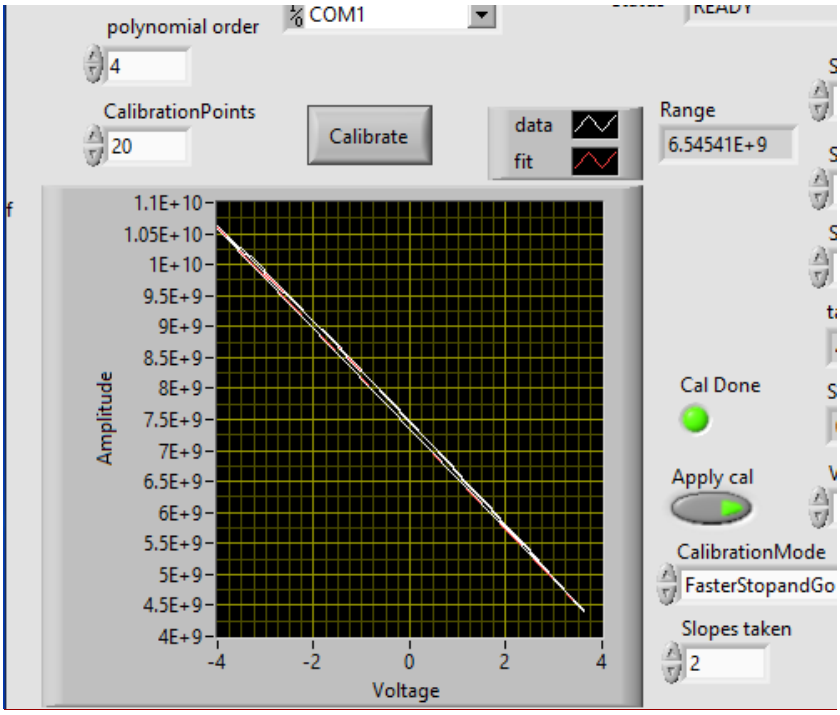

Figure 9. Front Panel GUI elements for the calibration protocol. Clicking "Calibrate" begins the calibration protocol. The calibration protocol consists of a stepwise function: the voltage output from the DAQ to the probe laser is increased linearly. At each discrete voltage, the beat frequency of the pump and probe laser is computed by the Keysight Signal Analyzer and then read by LabVIEW via a VISA command sent through the USB. The relationship between voltage sent to the probe laser and beat frequency is found through a fitting procedure. The user can adjust the number of calibration slopes taken and then fitted using the "Slopes taken" control. The fitting function used is a polynomial, whose degree can be controlled by the "polynomial order" control. The number of discrete voltages the DAQ outputs to the probe laser is controlled by the "CalibrationPoints" control. The "Range" indicator informs the user of the range of frequencies obtained during the calibration. Due to laser drifting between acquisitions and the nonlinear relationship between voltage passed through the probe's ARC and the probe's actual frequency, the automation of this module was a paramount concern, as calibration had to be executed prior to any given acquisition to maintain integrity and repeatability of results.

2.3.3 Acquisition Protocol

The Acquisition case is the dedicated case for synchronizing and acquiring data. When this case is activated by clicking the "Acquire and save" button on the front panel, most GUI functionality is disabled to maintain the integrity of the acquisition. During the Run case, the user may designate one of three modes of acquisition and adjusts a number of parameters for each mode (Figure 10). When a spectral scan is triggered during the acquisition, a subVI module

is executed. Via niDAQ library calls, the DAQ initiates a voltage scan while simultaneously reading the analog input of both the DC voltage and the SBS signal.

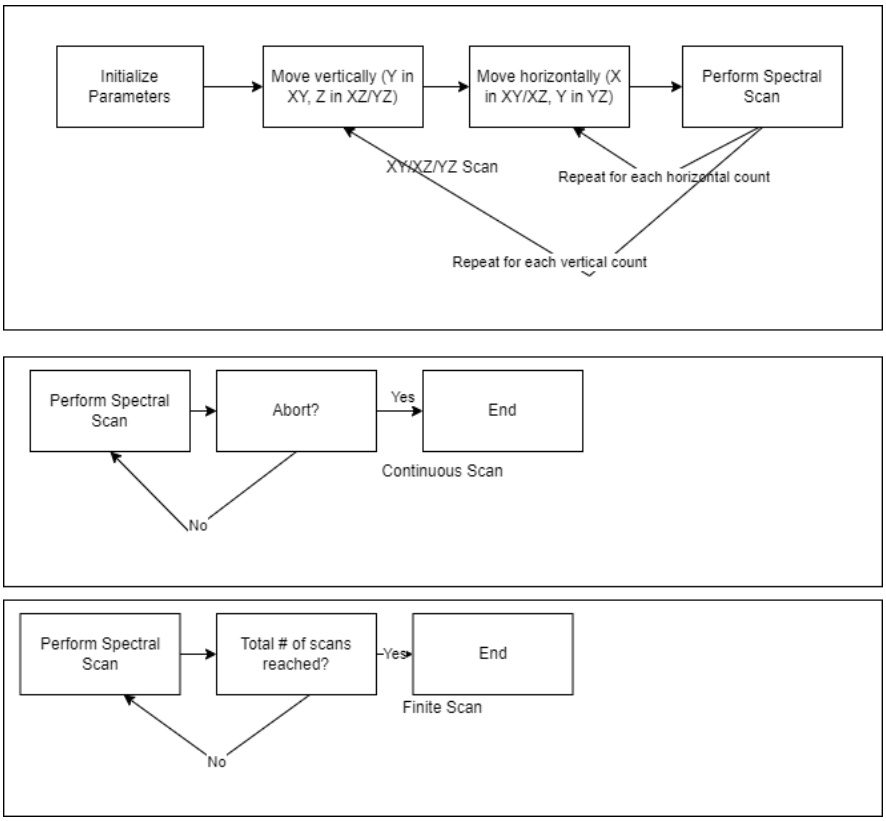

Figure 10. Diagram of the 3 main modes of acquisition. In the XY/XZ/YZ scan mode, the stage performs a raster scan in the XY/XZ/YZ plane using inputted parameters such as the number of steps in each direction, and the spatial distance between each step. The user chooses which plane to scan in before the acquisition begins. The continuous scan mode performs a spectral scan until the acquisition is aborted by a front panel button. The finite scan mode takes N number of spectral scans, where N is inputted as a parameter before the acquisition begins.

Regardless of the mode of acquisition, the architecture of the acquisition is largely the same. Data saved from each individual spectral scan flows from the acquisition protocol loop into the Data IO loop, where it is post processed (Figure 11). Spectra are fitted with a Lorentzian function using a MATLAB script embedded in the block diagram, and the resulting fitting parameters are

saved as a .mat file and/or excel file, contingent on user input. All raw spectral data is saved as a TDMS file (Figure 12).

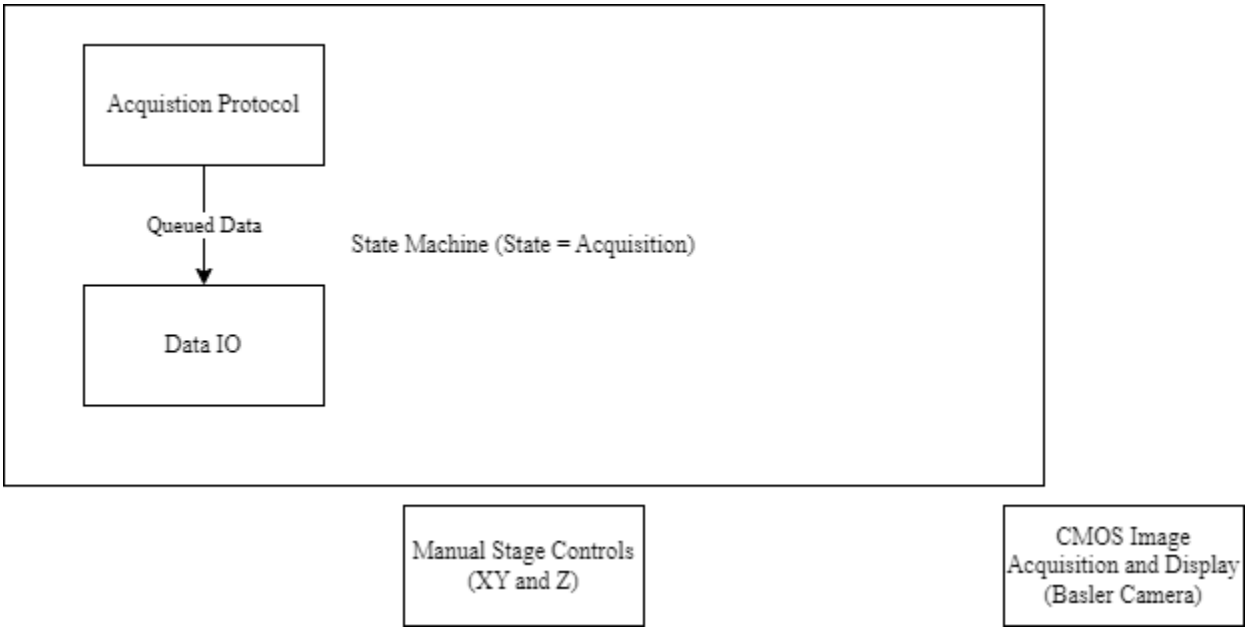

Figure 11. Diagram of the acquisition case. Each box represents a while loop, labels designating the functions of that loop. The acquisition protocol acquires the raw data and passes it through an enqueue element. The data is dequeued in the Data IO loop, where it is post processed and saved. In this architecture, the Acquisition Protocol loop runs parallel to the Data IO loop; this ensures that the speed of data processing does not affect the speed of acquisition.

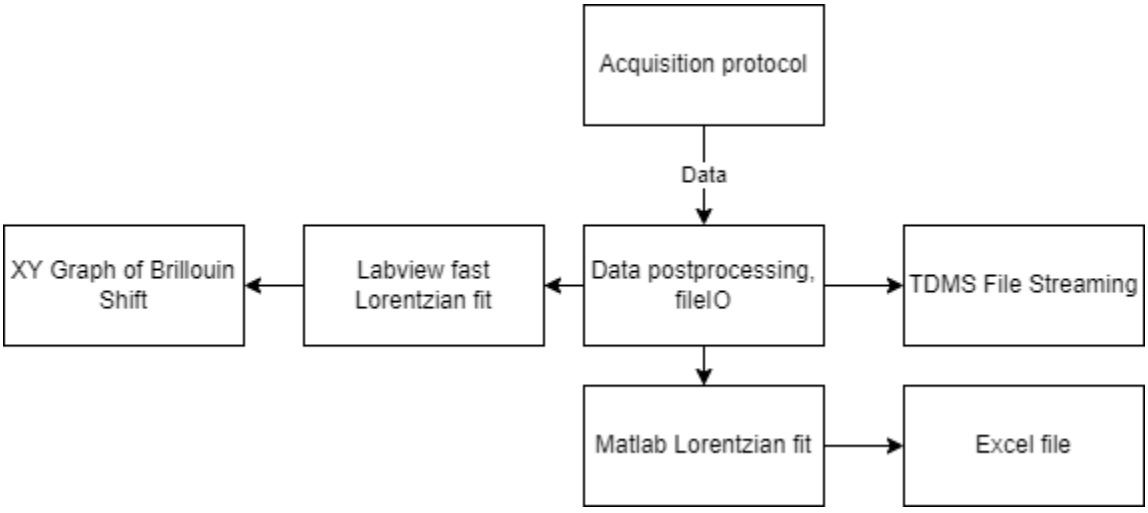

Figure 12. Data IO loop diagram. Arrows indicate the flow of data.

Depending on if the mode of acquisition is set to scan the XY plane, a fast Lorentzian fit, calculated natively through LabVIEW, is used to compute the peak position of the Lorentzian, which is then mapped to the corresponding XY coordinate in an intensity graph (Figure 13).

Regardless, at the end of the acquisition, the case reverts to the Run case.

Clicking on the “Close and Exit” button causes the state machine to switch to the Exit case, where instrument connections are closed and memory is deallocated.

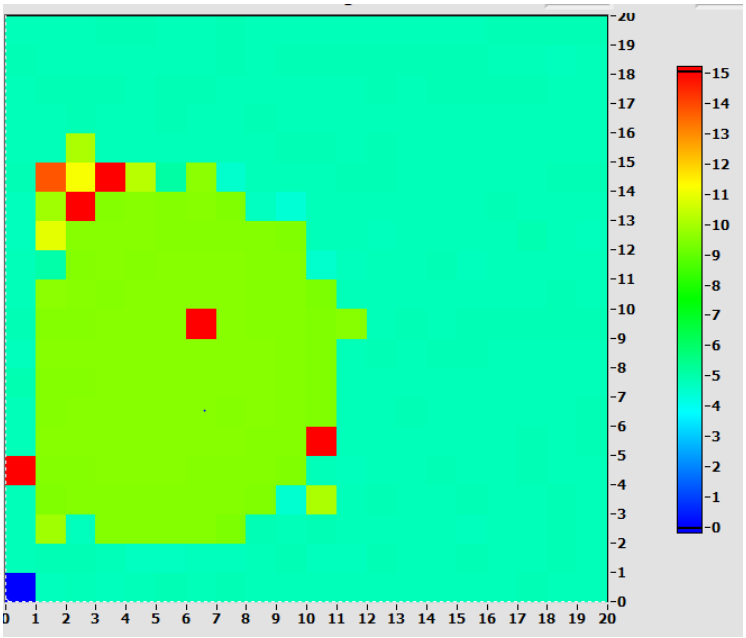

Figure 13. XY Brillouin shift map. In this graph, the Brillouin shift of a polystyrene bead in water is mapped in the XY plane. Polystyrene has a characteristic Brillouin shift of 9.5 GHz, while water of 5.1 GHz.

3. Implementation of Localization Theory

3.1 Measuring Spectra

Enabled by the novel LabVIEW automation, the theorized benefits of localization theory to SNR and acquisition time were realized experimentally. Water placed in a dish under the microscopy setup was used as test sample and its Brillouin spectrum was acquired using parameters consistent with demonstrating the application of the theory (Zanini & Scarcelli, 2022). 100 water spectra were scanned at both 5 and 50 ms acquisition time for each spectral channel size condition.. Spectra were acquired at constant pump and probe powers (160 and 10 mW, respectively), fitted by a Lorentzian function in MATLAB, and their characteristics were extracted for plotting (Figure 14).

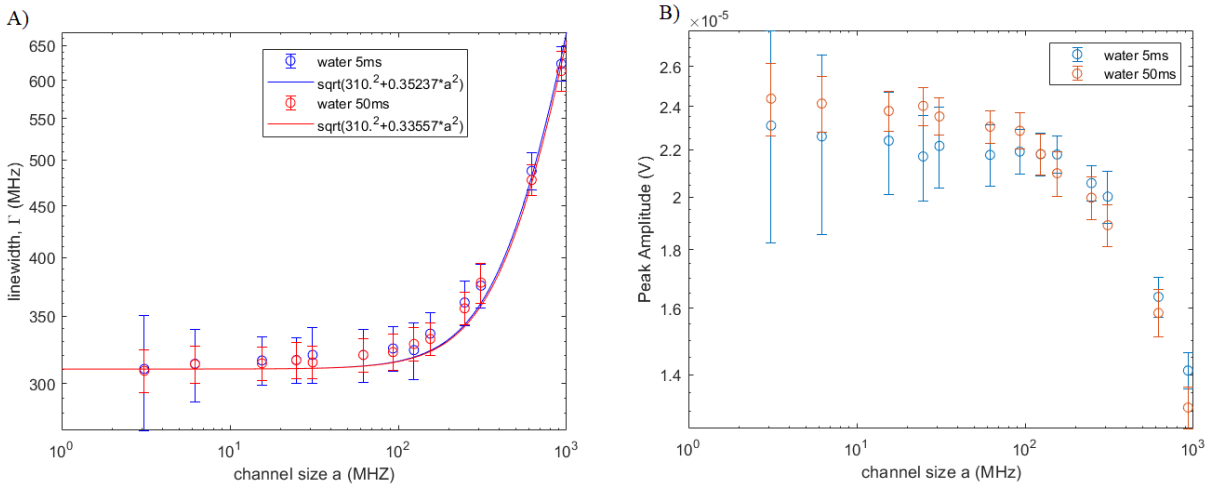

Figure 14. Demonstration of effect channel size has on spectral parameters. A) Linewidth of spectra acquired at 5 ms and 50 ms acquisition time while varying the spectral channel size a. Data is fitted to equation 8 (solid lines). B) Peak amplitude of the spectra acquired at each channel size. The broadening effect can be observed as the channel size becomes larger and the peak becomes more difficult to localize due to linewidth increasing as the peak amplitude decreases, leading to a flattening of the spectra.

To experimentally demonstrate the improved peak localization with channel size optimization, the measured shift precision, computed as standard deviation of the fitted peak location over the

100 repetitions, was fitted to equation 7 (Figure 15) using the broadening factor B computed from data presented in Figure 14.

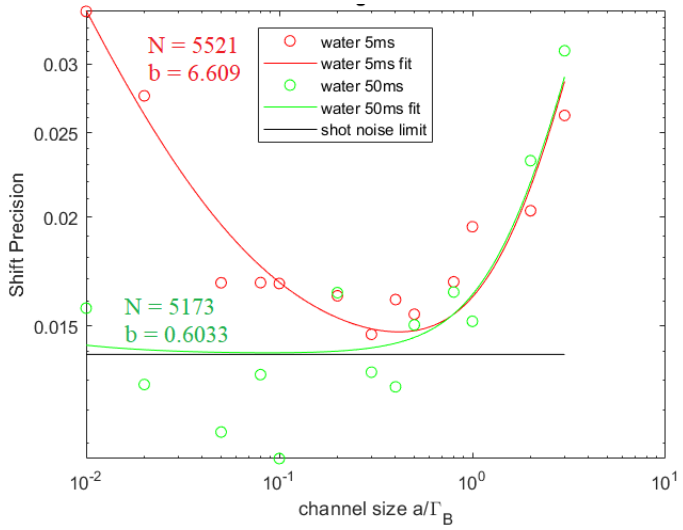

Figure 15. Experimental plot of calculated shift precision versus the normalized channel size for 5 ms (red) and 50 ms (green) acquisition time.

Consistent with localization theory, precision improves as a result of larger channel sizes due to the acquisition of more photons per channel; the subsequent loss in precision is due to the pixelation noise resulting from the broadening effect.

A likewise improvement of SNR is observed when channel size is optimized (Figure 16). At a constant acquisition time of 5 ms, the SNR of the signal increases by a factor of $\sqrt{40}$ upon 40 times increase of the channel up to its optimal size, following a log-linear relationship. Similarly, when SNR was kept constant by keeping the τ_{LIA} constant, acquisition speed was increased by 25x (from 50 ms to 2 ms) while increasing the channel 25 times, without sacrificing SNR.

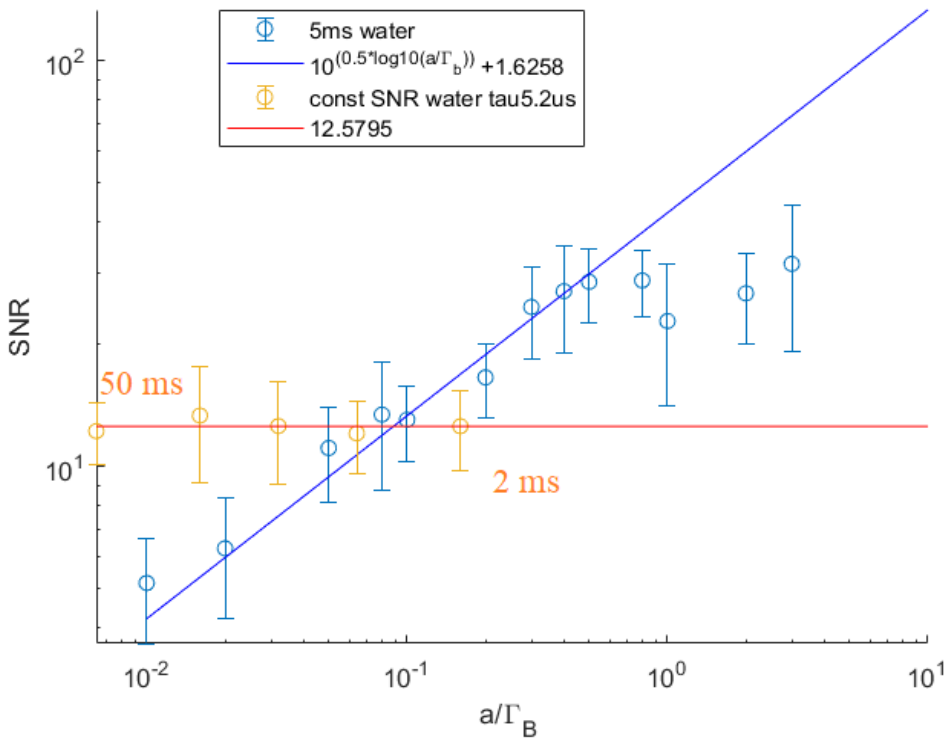

Figure 16. Plot of SNR versus normalized channel size for two conditions: constant acquisition time of 5 ms (blue), and constant SNR maintained by keeping the τ_{LIA} constant at 5.2 microseconds (yellow). The leftmost datapoint taken from a constant τ_{LIA} was acquired at 50 ms acquisition time; the rightmost datapoint was taken at 2 ms acquisition time.

Combined, these results demonstrate the ability localization theory has for optimizing and improving also SBS spectral measurements, and further demonstrate the efficiency and robustness that the LabVIEW instrumentation offers.

3.2 Microfluidics

Following from previous work published, an attempt was made to leverage the faster acquisition time of the novel SBS spectrometer for use in flow cytometry (Zhang et al., 2017). To replicate the experimental setup, a 100 x 100 micron microfluidic chip (Straight 4-channel Mini-Luer Chip, Chipshop) was placed onto the sample stage, and brought into focus looking at the CMOS camera image. The chip was connected to a syringe pump via a series of mini luer connectors

and tubing. In order to demonstrate the system's ability to acquire spectra of elements within a microfluidic channel at speeds 10x faster than previous work, water was pumped via the syringe pump into the channel, and spectra were acquired at an acquisition time of 5 ms. Subsequently, the syringe pump was refilled with methanol and pumped through the channel, with spectra being continuously acquired. Finally, the syringe pump was refilled with water again, and pumped through, with spectra being once again continuously acquired (Figure 17).

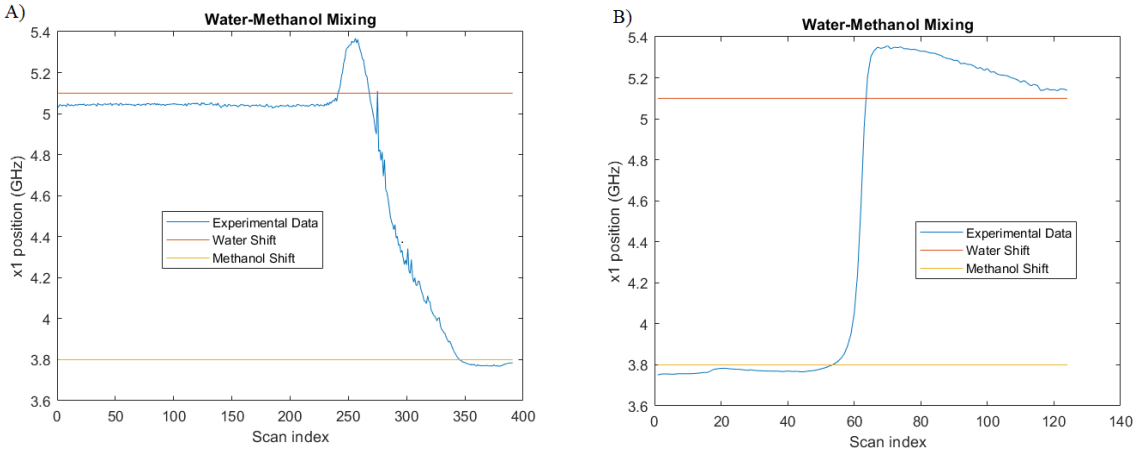

Figure 17. Water-methanol flow experiments in the microfluidic channel, with Brillouin peak position plotted against the number of consecutive scans taken, all spectra being acquired in a 5 ms acquisition time. A) Water in the channel being replaced by methanol. B) Methanol in the channel being replaced by water.

Elevations in the Brillouin shift above the expected shift for water (5.1 GHz) follows literature about water-methanol mixing behavior (Mijaković et al., 2011). Water-methanol mixing is a nonideal phenomenon, which leads to greater packing of molecules, changing the thermodynamic properties of the mixture and therefore leading to an increase in the observed Brillouin shift. Regardless, these results demonstrate the capacity of the instrument to acquire at ~10x the acquisition speed of traditional spontaneous Brillouin spectroscopy within a microfluidic channel (5ms instead of 50 ms).

3. Conclusion

Here, we present a novel instrumentation scheme orchestrated and synchronized by a LabVIEW automation program. We experimentally confirmed the acquisition of SBS spectra and demonstrated the use of localization theory in practice to increase acquisition speed and/or SNR of the spectra. The LabVIEW virtual instrument proved necessary and efficient for the realization of this localization theory, as it synchronized and acquired spectra in a user-friendly GUI with a high number of parameters being able to be easily controlled on the front panel. As a standalone application, the virtual instrument can be operated for any number of possible future acquisitions using the optical setup previously discussed. One possible future project this instrumentation and acquisition scheme could be used for is in a more direct attempt at Stimulated Brillouin Flow Cytometry.

Apart from the water-methanol flow previously discussed, additional microfluidic experiments attempted to replicate the previous work in flow cytometry more directly. Polydispersed polystyrene beads (10-13 micron diameter) were flowed through the microfluidic channel using the syringe pump set to a flow rate of 0.005 μL/min, and attempts were made to perform a line scan of the bead (Brillouin shift of 9.5 GHz) similar in protocol to previous Brillouin flow cytometry literature (Zhang et al., 2017). The beads were able to flow through the microfluidic channel, be observed with the CMOS indicator (Figure 3), and have spectra extracted and acquired. However, due to the high pump power (180 mW), optical trapping of the bead was observed (Neuman & Block, 2004), leading to the inability to perform a line scan of the bead. A fruitful future direction would be to minimize this optical trapping phenomena, as then the throughput of the flow cytometer would be increased by a factor of ~10 due to the increased spectral acquisition speed. With the preprogrammed acquisition modes and easily

tunable scanning parameters, the LabVIEW program would require virtually no adjustments for use in this application.

Bibliography

Benghanem, M. (2009). Measurement of meteorological data based on wireless data acquisition system monitoring. Applied Energy, 86(12), 2651–2660. https://doi.org/10.1016/j.apenergy.2009.03.026

Berghaus, K. V., Yun, S. H., & Scarcelli, G. (2015). High Speed Sub-GHz Spectrometer for Brillouin Scattering Analysis. Journal of Visualized Experiments : JoVE, 106, 53468. https://doi.org/10.3791/53468

Boyd, R. W. (2020). Chapter 8—Spontaneous Light Scattering and Acoustooptics. In R. W. Boyd (Ed.), Nonlinear Optics (Fourth Edition) (pp. 381–417). Academic Press. https://doi.org/10.1016/B978-0-12-811002-7.00017-5

Brillouin, L. (1922). Diffusion de la lumière et des rayons X par un corps transparent homogène—Influence de l'agitation thermique. Annales de Physique, 9(17), Article 17. https://doi.org/10.1051/anphys/192209170088

Deschout, H., Zanacchi, F. C., Mlodzianoski, M., Diaspro, A., Bewersdorf, J., Hess, S. T., & Braeckmans, K. (2014). Precisely and accurately localizing single emitters in fluorescence microscopy. Nature Methods, 11(3), Article 3. https://doi.org/10.1038/nmeth.2843

Elliott, C., Vijayakumar, V., Zink, W., & Hansen, R. (2007). National Instruments LabVIEW: A Programming Environment for Laboratory Automation and Measurement. JALA: Journal of the Association for Laboratory Automation, 12(1), 17–24. https://doi.org/10.1016/j.jala.2006.07.012

Giannone, L., Eich, T., Fuchs, J. C., Ravindran, M., Ruan, Q., Wenzel, L., Cerna, M., & Concezzi, S. (2011). Data acquisition and real-time bolometer tomography using

LabVIEW RT. Fusion Engineering and Design, 86(6), 1129–1132. https://doi.org/10.1016/j.fusengdes.2011.03.119

Handler, C., Scarcelli, G., & Zhang, J. (2023). Time-lapse mechanical imaging of neural tube closure in live embryo using Brillouin microscopy. Scientific Reports, 13. https://doi.org/10.1038/s41598-023-27456-z

Kodosky, J. (2020). LabVIEW. Proceedings of the ACM on Programming Languages, 4(HOPL), 78:1-78:54. https://doi.org/10.1145/3386328

Mijaković, M., Kežić, B., Zoranić, L., Sokolić, F., Asenbaum, A., Pruner, C., Wilhelm, E., & Perera, A. (2011). Ethanol-water mixtures: Ultrasonics, Brillouin scattering and molecular dynamics. Journal of Molecular Liquids, 164(1), 66–73. https://doi.org/10.1016/j.molliq.2011.06.009

Neuman, K. C., & Block, S. M. (2004). Optical trapping. Review of Scientific Instruments, 75(9), 2787–2809. https://doi.org/10.1063/1.1785844

Nikolić, M., & Scarcelli, G. (2019). Long-term Brillouin imaging of live cells with reduced absorption-mediated damage at 660nm wavelength. Biomedical Optics Express, 10(4), 1567–1580. https://doi.org/10.1364/BOE.10.001567

Remer, I., & Bilenca, A. (2016). High-speed stimulated Brillouin scattering spectroscopy at 780 nm. APL Photonics, 1(6), 061301. https://doi.org/10.1063/1.4953620

Remer, I., Shaashoua, R., Shemesh, N., Ben-Zvi, A., & Bilenca, A. (2020). High-sensitivity and high-specificity biomechanical imaging by stimulated Brillouin scattering microscopy. Nature Methods, 17(9), Article 9. https://doi.org/10.1038/s41592-020-0882-0

Scarcelli, G., Kim, P., & Yun, S. H. (2011). In Vivo Measurement of Age-Related Stiffening in the Crystalline Lens by Brillouin Optical Microscopy. Biophysical Journal, 101(6),

1539–1545. https://doi.org/10.1016/j.bpj.2011.08.008

Scarcelli, G., Polacheck, W. J., Nia, H. T., Patel, K., Grodzinsky, A. J., Kamm, R. D., & Yun, S. H. (2015). Noncontact three-dimensional mapping of intracellular hydromechanical properties by Brillouin microscopy. Nature Methods, 12(12), Article 12. https://doi.org/10.1038/nmeth.3616

Scarcelli, G., & Yun, S. H. (2008). Confocal Brillouin microscopy for three-dimensional mechanical imaging. Nature Photonics, 2(1), Article 1. https://doi.org/10.1038/nphoton.2007.250

Scarcelli, G., & Yun, S. H. (2011). Multistage VIPA etalons for high-extinction parallel Brillouin spectroscopy. Optics Express, 19(11), 10913–10922. https://doi.org/10.1364/OE.19.010913

Thinh, T. N. H., Lam, P. D., Tran, H. Q., Tien, L. H. C., & Thai, P. H. (2023). Transformer vibration and noise monitoring system using internet of things. IET Communications, n/a(n/a). https://doi.org/10.1049/cmu2.12585

Thompson, R. E., Larson, D. R., & Webb, W. W. (2002). Precise Nanometer Localization Analysis for Individual Fluorescent Probes. Biophysical Journal, 82(5), 2775–2783. https://doi.org/10.1016/S0006-3495(02)75618-X

Zanini, G., & Scarcelli, G. (2022). Localization-assisted stimulated Brillouin scattering spectroscopy. APL Photonics, 7(5), 056101. https://doi.org/10.1063/5.0087697

Zhang, J., A. Nou, X., Kim, H., & Scarcelli, G. (2017). Brillouin flow cytometry for label-free mechanical phenotyping of the nucleus. Lab on a Chip, 17(4), 663–670. https://doi.org/10.1039/C6LC01443G

Zhang, J., & Scarcelli, G. (2021). Mapping mechanical properties of biological materials via an

add-on Brillouin module to confocal microscopes. Nature Protocols, 16(2), Article 2. https://doi.org/10.1038/s41596-020-00457-2

Zhi-yu, S. (2016). Realization of the motor data acquisition and analyzation system based on the producer/consumer model of LabVIEW. 2016 IEEE Advanced Information Management, Communicates, Electronic and Automation Control Conference (IMCEC), 330–334. https://doi.org/10.1109/IMCEC.2016.7867227